Non-destructive detection and analysis of weld defects in dissimilar pulsed GMAW and FSW joints of aluminium castings and plates through 3D X-ray computed tomography

(Article begins on next page)

ORIGINAL ARTICLE

Non-destructive detection and analysis of weld defects in dissimilar pulsed GMAW and FSW joints of aluminium castings and plates through 3D X-ray computed tomography

Mattia Orlando[1] · Manuela De Maddis[1] · Valentino Razza[1] · Vincenzo Lunetto[1]

Abstract

This work focuses on porosity formation during the welding of dissimilar aluminium alloys (cast and sheet) by pulsed gas metal arc welding (GMAW) with different travel speeds (12–14 mm/s) and by friction stir welding (FSW). The case study concerns the assembling of a battery-pack enclosure prototype. The welded specimens were scanned by 3D X-ray computed tomography. The cast base material (BM) shows a porosity percentage of 1.45%, and it is characterized by pores with a strong hyperbolic relationship between equivalent diameter and sphericity. Considering the GMAW beads, porosity rises with the travel speed (from 1.80 to 5.12%), due to the reduction of the opening window in which pores can escape. Pores with volume higher than 0.10 mm^3 rise with the travel speed, representing from 9.75 to 32.98% of the total porosity. These pores are responsible for the weaker hyperbolic connection for sphericity found for the GMAW beads. On the other hand, FSW mixes and homogenizes the pores in the cast BM. The novelty of the paper lays in proving the strong potentialities of FSW for weld porosity reduction. A re-designing of the battery-pack enclosures is necessary to limit arc welding in marginal areas, which are not crucial for sealing but necessary to create a stable platform to be subsequently sealed with FSW.

Keywords Battery-pack enclosure · Electric vehicles · Friction tool · Porosity · Sphericity · Sustainable mobility

1 Introduction

According to the outlooks reported in Ref. [1], electric vehicles (EVs) will account for over 10% of the road vehicle fleet by 2030. Total EV sales will reach over 20 million in 2025 and over 40 million in 2030, representing respectively over 20% and 30% of all vehicle sales. The lithium-ion battery pack is the most common powertrain solution for EVs [2, 3]. However, Lu et al. [4] highlighted that this kind of power source entails different safety issues due to mechanical vibration of transmission, external load shock and thermal runaway. The enclosure parts should be assembled to ensure thermal and electrical insulation and a high sealing level [5], as well as weight reduction, high minimum natural frequency and structural strength [6].

In this scenario, the use of aluminium alloys is growing due to their good strength-to-mass ratio, excellent formability and excellent corrosion resistance [7]. A DuckerFrontier study published at the end of 2019 showed that the average aluminium content in EU cars is about 179 kg, of which 116 kg comes from casting [8]. For instance, the luxury electric GM Cadillac's battery housing is manufactured using stamping and high-pressure die casting (HPDC) of aluminium alloys. Novelis designed a new AA6xxx series alloy, which is implemented in the Jaguar Land Rover I-PACE [9]. Nowadays, it is clear that assembling between cast and wrought (e.g. sheets or extruded products) aluminium alloys is a method for large-scale lightweight chassis and battery-pack enclosure construction. Different assembling technologies are implemented in such applications. Modularity is a characteristic of battery packs thanks to the stackable form of prismatic cells. Therefore, mechanical nut and bolt fasteners or clip fitting are implemented when modularity and easy disassembly are necessary [10]. On the other hand, welding processes are mainly used for structural assembling to guarantee a high sealing level [5].

✉ Vincenzo Lunetto
vincenzo.lunetto@polito.it

1 Department of Management and Production Engineering, Politecnico Di Torino, Corso Duca Degli Abruzzi 24, 10129 Turin, Italy

Thermal technologies such as gas metal arc welding (GMAW) can promote porosity, especially in aluminium cast alloys [11]. On the other hand, friction stir welding (FSW) can mitigate this phenomenon thanks to its solid-state nature [12, 13]. Tagawa et al. [14] compared the properties of A356-T6 butt joints obtained with GMAW and FSW. The BM showed a hardness of 100 HV, which dropped to 70 HV and 50 HV, respectively, after the solid-state and thermal welding technology. Abdollahzadeh et al. [15] proposed two variations of conventional FSW, namely friction stir vibration welding (FSVW) and underwater friction stir welding (UWFSW), and performed a comparison on AA6061-T6 joints. The weld efficiency of the UWFSW joints was around 89%, while this value was about 82% and 77% for FSVW and CFSW joints, respectively. Moreover, Abdollahzadeh et al. [16] obtained a grain size in the stir zone (SZ) of FSVW joints produced with water cooling equal to 13% of that in the BM thanks to the application of vibration and cooling system. FSVW showed also advantages in improving the formability of aluminium tailor welded blanks (TWB) produced by FSW [17, 18]. For instance, superior strength, hardness and ductility were measured for FSVW blanks in comparison to FSW samples due to the more intensified dynamic recrystallization (DRX) in the FSVW process which resulted in finer grains.

This work investigates the dissimilar welding of cast and sheet aluminium alloy parts to assemble battery-pack enclosure prototypes. The paper aims to highlight the distribution, dimension and shape (i.e. spherical and irregular) of porosity throughout the weldments carried out via pulsed GMAW, while varying the torch travel speeds and assessing the effect of the different base materials (BMs). The specimens were scanned by 3D X-ray computed tomography (CT). This study also compares pulsed GMAW with the FSW technology concerning the same joint application. This work aims to highlight if a redesign of the battery-pack enclosure prototype is necessary or not considering the different sealing levels obtained with GMAW and FSW.

1.1 Mechanisms of porosity formation in aluminium welds

According to Vyskoč et al. [19], macroporosity is represented from pores with a size above 300 μm. Below this value, pores are normally considered as microporosity. Microporosity is mainly caused by the shrinkage associated with the metal solidification and air trapping. These defects are generally so small that their influence on joint strength is negligible, while their effect can be notable under dynamic loading conditions. On the other hand, macroporosity is mainly caused by the different hydrogen solubility in liquid and solid aluminium [20]. This paragraph reports a state-of-the-art literature review on the causes of macroporosity formation during thermal welding of aluminium alloys.

Hydrogen solubility at the melting point of pure aluminium is rather high, 6.32×10^{-5} wt. % H (i.e. 0.71 cm^3/100 g) [21]. Hydrogen solubility reduces to 3.81×10^{-6} wt. % H (i.e. 0.043 cm^3/100 g) when aluminium melt-pool changes from liquid to solid state [22]. As a result, hydrogen nucleates as bubbles during weld solidification and can remain entrapped as pores [23]. Hydrogen solubility in solid aluminium changes with chemical alloying. For instance, magnesium reduces hydrogen solubility, increases the concentration of supersaturated hydrogen at the liquid–solid interface and favours the formation of a larger number of hydrogen bubbles in the melt-pool [24]. Vyskoč et al. [19] have found that the addition of 5% He in the Ar shielding gas reduced weld porosity from 0.08% (pure argon) to below 0.05%. Similarly, Liu et al. [25] measured a porosity reduction from 5% (pure argon) to 0.5% using a shielding gas composed of 39% Ar + 1% CO_2 + 60% He. Hwang et al. [11] observed that increasing the argon flow rate from 8 to 22 l/min could reduce the number of pores dramatically. The same authors showed that the chemical composition of filler material (e.g. ER4043, ER5356, ER5556) plays a role in macroporosity formation. Chen et al. [23] investigated the influence of tilt arc angle on the weld porosity. Porosity decreased by increasing the tilt angle from 0° to 35°, measuring a cumulative pore volume reducing from 1.5 to 0.2 mm^3. The authors stated that if the arc is inclined, a horizontal force component stirs the molted metal through a longer path, thus facilitating the growth and the successive overflow of hydrogen bubbles.

As the best of the authors' knowledge, the state-of-the-art literature shows a lack of studies on the effect of the travel speed in porosity formation in GMAW joints. This work fills this gap quantifying porosity by means of the CT analysis.

2 Materials and methods

This work investigates dissimilar welding of AlSi9MgMn casting (T64 condition) with a 3-mm-thick sheet of 6HS s650 (T6 condition). AlSi9MgMn alloy is one of the most performant cast aluminium alloys for the automotive market [26, 27]. The 6HS s650 alloy is a recent high-strength AA6xxx series used for structural applications requiring high in-service strength [9]. An AlMg5 filler wire (AWS ER5356 grade) with a diameter of 1.2 mm was used during the welding operation according to the recommendations of ISO 18273 standard [28]. The chemical composition and the nominal mechanical properties of the selected materials are listed in Tables 1 and 2, respectively.

Single-side T-joints between AlSi9MgMn and 6HS s650 were obtained by direct current pulsed GMAW welding,

**Table 1** Nominal chemical composition in wt. % (Al. balanced)

Alloy	Si	Fe	Mn	Cu	Mg	Cr	Zn	Ti
AlSi9MgMn [27]	9.5–11.5	0.15	0.50–0.80	0.03	0.10–0.50	-	0.07	0.04–0.15
6HS s650 [9]	0.6–0.9	<0.40	0.05–0.25	0.6–0.9	0.7–1.0	0.05–0.20	<0.25	<0.10
ER5356 [29]	<0.25	<0.40	0.05–0.20	<0.10	4.5–5.5	0.05–0.20	<0.10	0.06–0.20

Table 2 Nominal mechanical characteristics of the selected materials

Mechanical property	AlSi9MgMn [27]	6HS s650 [9]	ER5356 [29]
Tensile strength	279 MPa	370–390 MPa	200–310
Yield strength	133 MPa	330–350 MPa	80–200
Elongation at fracture	9.5%	≥12%	-

as shown in Fig. 1. The welding system consisted of an industrial six-axis anthropomorphic robot equipped with an electrical generator Fronius mod. Trans Puls Synergic 400i welding machine. The Al components were first polished with a stainless-steel brush to remove superficial oxide films and then cleaned with acetone. The welding parameters were selected based on a preliminary literature review on dissimilar aluminium (casting and plate) joints, followed from preliminary pilot experiments and the authors' experience. Studies [30–32] refer to BMs with a thickness comparable to that used in this study. A minimum of 6–8 mm/s and a maximum of 16 mm/s were used for the travel speed. However, in this study, the minimum level was fixed to 12 mm/s to meet the productivity requirements of the case study. On the other hand, the maximum level was limited to 14 mm/s to avoid lack of penetration, which would have compromised the high sealing level requested for battery EVs. As Li et al. [30] recommended, the torch position was kept constant at an inclination of 15° to the perpendicular of the sheet. An inclination of 40° was maintained with respect to the cast part. The other process parameters (Table 3) were adapted during preliminary pilot experiments following the two following constraints: (i) the visual aspect of the joint, especially referring to the porosity at the connection borders between weld and BMs, and (ii) the penetration of the weld inside the BMs. Pure argon with a flow rate of 12 l/min was used

Fig. 1 Schematic of the Single-side T-joints between AlSi9MgMn casting (blue) and 6HS s650 plates (grey) and GMAW torch position
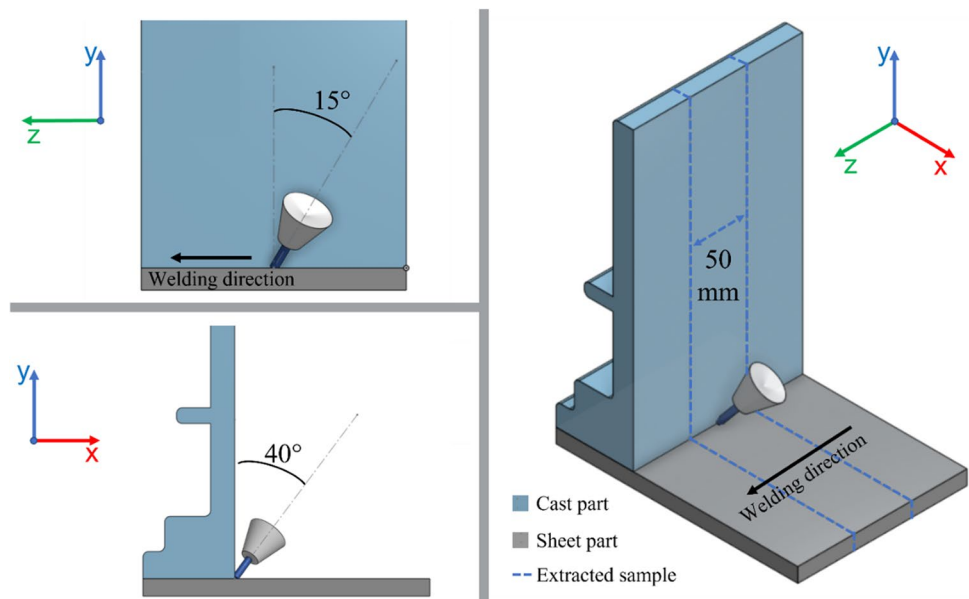
Table 3 Process parameters for the direct current pulsed GMAW welding

Specimens	Travel speed	Peak current	Wire feed speed	Gas flow rate	Pulse frequency	Pulse duty cycle
#1	12 mm/s	190 A	11 m/min	12 l/min	3 Hz	50%
#2	13 mm/s					
#3	14 mm/s					

as shielding gas. Three welding repetitions were performed for each travel speed. After welding, 50-mm-long specimens were obtained by removing the two ends of the weld for the non-destructive test through CT (Fig. 1).

Samples were also extracted from the welded joints for microstructural and hardness examinations. The metallographic samples were prepared to a standard grinding and polishing, and then etched with a Keller's reagent according to the ASTM E-407 standard. The weld microstructure has been assessed with an optical microscope. The weld geometry has also been determined, including fillet size, bead width, penetration depth at the casting and plate sides. Vickers microhardness measurements were conducted with a 100-g load and 15-s dwell time according to the ASTM E92 standard [33]. An incremental step of 400 μm was used throughout the cross-section of the joint to build a microhardness map with MATLAB software.

The AlSi9MgMn and 6HS s650 were also welded through FSW in lap joint configuration. The experimental setup is displayed in Fig. 2a. The FSW joint was welded using a 100 kN FSW machine with a water-cooled spindle available at the interdepartmental laboratory J-Tech of Politecnico di Torino. The tool had a flat shoulder and a truncated pyramid thread pin (square base and tip). A pin length of 4 mm was selected with the aim to meet the plate thickness and to produce a SZ deep enough inside the cast BM. After a preliminary investigation, the following welding parameters were selected: rotational speed 1200 rpm, travel speed 500 mm/min, plunge depth 4.15 mm, dwell time 3 s. In this study, priority was given to productivity limiting the travel speed only to avoid tunnel or groove-like defects, which would have compromised the sealing level requested. Three welding repetitions were performed. After welding, samples with a length of 50 mm were extracted from the welded

joint; Fig. 2a shows the cross-section and subjected to the tomographic examination. Metallographic samples were also extracted from the weld seams to perform microstructural and hardness examination through the same procedures used for the GMAW samples.

The CT analysis was conducted on the GMAW beads and FSW joints to detect defects, their size, and shapes when welding Al casting and plates together through fusion and solid-state welding. This analysis was also conducted on the cast part to evaluate the condition of this BM. The non-destructive tests were performed with the tomographic equipment with a maximum operating voltage of 300 kV and resolution of 5 μm. The CT equipment is present at the interdepartmental laboratory J-Tech of Politecnico di Torino, and it can scan samples with dimensions up to $500 \times 500 \times 500$ mm³. The system has a 4-axis worktable to manipulate the sample along the x–y-z directions and provide a 0–360° continuous rotation. The welded samples were examined with 270 kV voltage and 140 mA current. During the analysis, the sample rotated with steps of 0.225°, four projections were acquired in each position, and the average result was registered as a reference for that position. One thousand six hundred projections were acquired after completing a 360° rotation for the 3D reconstruction. The projections were processed by VGSTUDIO software, and the VGDefX algorithm was used to obtain detailed information about porosity in terms of position, size, sphericity and volume. The image resolution of 30 μm was the resolution for the cast BM and the FSW joint (sample size about 20.6 mm $\times$ 25.3 mm $\times$ 10.5 mm) and for the GMAW beads as well (sample size about 50 mm $\times$ 12 mm $\times$ 11 mm). The image resolution influences the capability of the VGDefX algorithm to detect pores. It cannot evaluate pores with a volume below four times
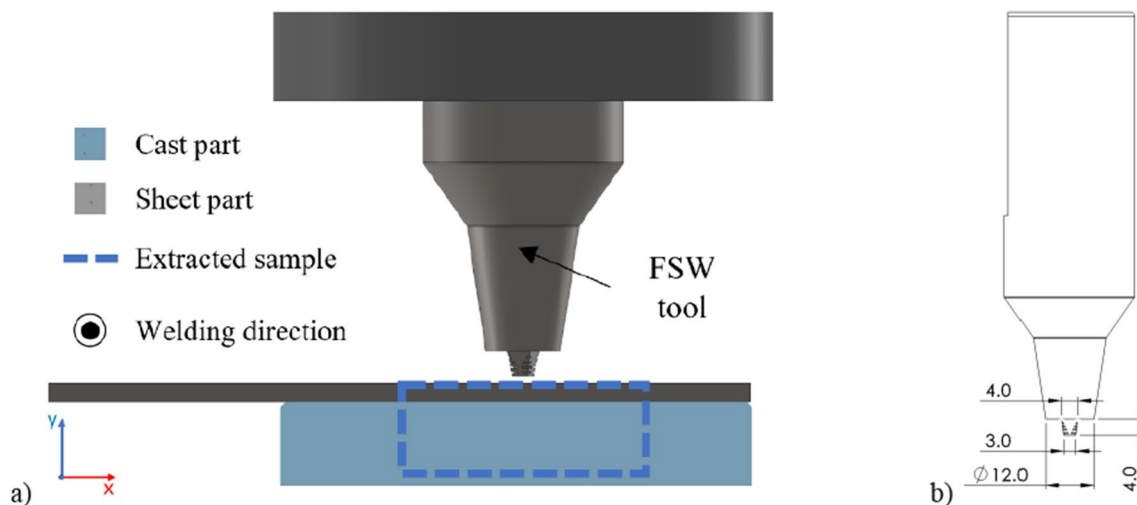

Fig. 2 FSW experimental campaign: **a** welding setup and **b** tool geometry (dimensions in [mm])

the volume of a cube with its side equal to the resolution. Therefore, the minimum volume of pore searched in this work was set to eight times the volume of this voxel. This volume equals 0.000216 mm^3 (i.e. 216,000 μm^3) in this study, corresponding to the minimum equivalent diameter of 0.07 mm by considering Eq. (2). The sphericity parameter (Ψ) was evaluated using Eq. (1) according to Wadell [34]. Pore sphericity is defined as the ratio between the surface area of a sphere (A_S) with the same volume as the pore (V_P) and the effective surface area of the pore (A_P). Moreover, the volume of the pore (V_P) can be used to calculate the equivalent diameter of a pore (d_{Eq}), as defined in Eq. (2):

$$\Psi = \frac{A_S}{A_P} = \frac{\pi^{1/3}(6 \cdot V_P)^{2/3}}{A_P} \tag{1}$$

$$d_{Eq} = 2 \cdot \sqrt[3]{\frac{3 \cdot V_P}{4 \cdot \pi}} \tag{2}$$

3 Results and discussion

3.1 GMAW joints

Figure 3 from a to c show the appearance of the GMAW joints for travel speed set to 12 mm/s, 13 mm/s and 14 mm/s, respectively. The weld seams are smooth and regular, even though some porosities are at the interface with the cast part. The cause of these defects can be associated with the intrinsic porosity of the casting, as discussed thereafter in paragraph 3.3. The weld size is influenced by the travel speed and, hence, by the rate of heat delivered per unit time. The weld dimensions are 6.38 mm and 6.28 mm along the y- and x-directions (refer to Fig. 1) at the lowest travel speed of 12 mm/s. As expected, they reduce to 6.23 mm and 5.49 mm and 6.00 mm and 5.30 mm when increasing travel speed at 13 and 14 mm/s, respectively. The weld depth is 1.52 mm, 0.97 mm and 0.90 mm, with a travel speed of 12 mm/s, 13 mm/s and 14 mm/s, respectively (Fig. 4). For the sake of clarity, Fig. 4 is not representative of the porosity

Fig. 3 Visual appearance of each sheet/cast GMAW joints carried out with a travel speed of **a** 12 mm/s, **b** 13 mm/s and **c** 14 mm/s
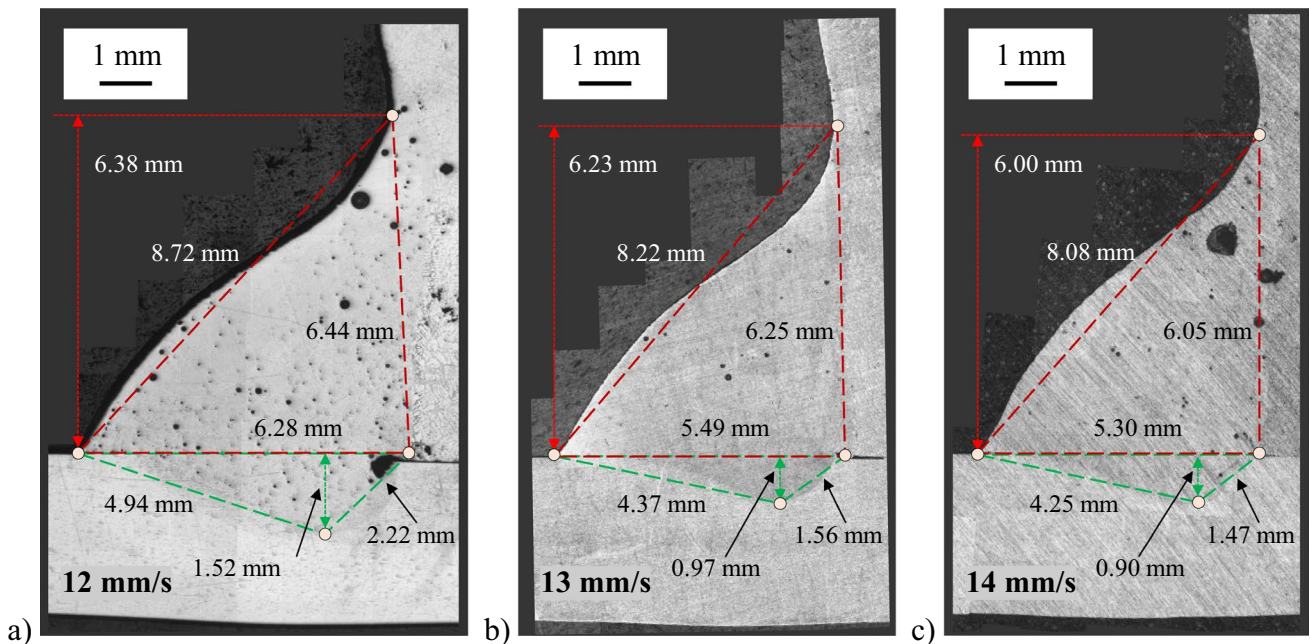

Fig. 4 Cross-section of each sheet/cast GMAW joints carried out with a travel speed of **a** 12 mm/s, **b** 13 mm/s and **c** 14 mm/s

distribution, because it derived from a single section of the weld bead, which will be instead evaluated over the complete welding path by CT.

Figure 5 shows the typical cross-section of an arc weldment, while the coloured marks highlight the locations of the microstructures reported in Fig. 6. The Al cast has the typical solidification structures that consist of dendrites surrounded by an Al–Si eutectic along their grain boundaries. The cast exhibits some pores caused by the foundry process (Fig. 6a). Likely, the cast, the welded bead exhibits some pores with a size in the range of 10–100 µm. However, they are more diffuse than those of the cast. The

higher travel speed reduces the power heat input and, hence, the extent of the welded region. The fuse zone (FZ) is characterized by a fine dendritic microstructure (dendrites length about 30 µm) in the centre of the weld (Fig. 6d). Al–Si eutectic is along the grain boundaries due to the high Si content of the cast. The weld microstructure progressively coarsens, moving to the sheet and cast parts (Fig. 6 e and c). The dendrite dimension rises to 100 µm and 300 µm in the heat-affected zone (HAZ) (Fig. 6b) and BM of the cast part (Fig. 5). At the sheet side, the HAZ recrystallized grains with an average size of 50 µm (Fig. 6e). The Al sheet shows elongated grains along the

Fig. 5 Cross-section of a sheet/cast GMAW weld carried out with a travel speed of 12 mm/s. The coloured marks highlight the locations of the microstructures reported in Fig. 6
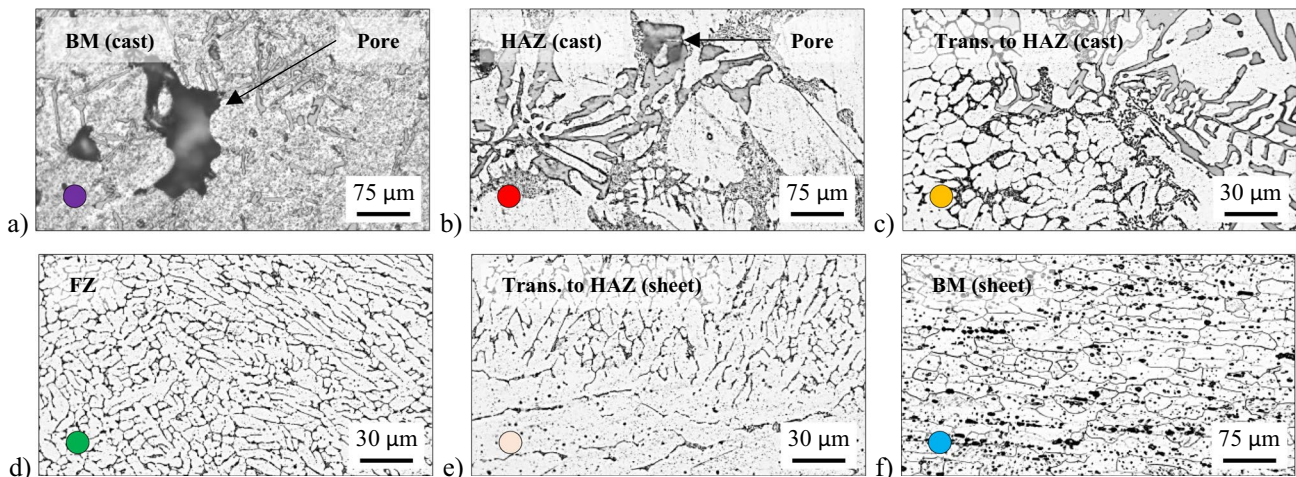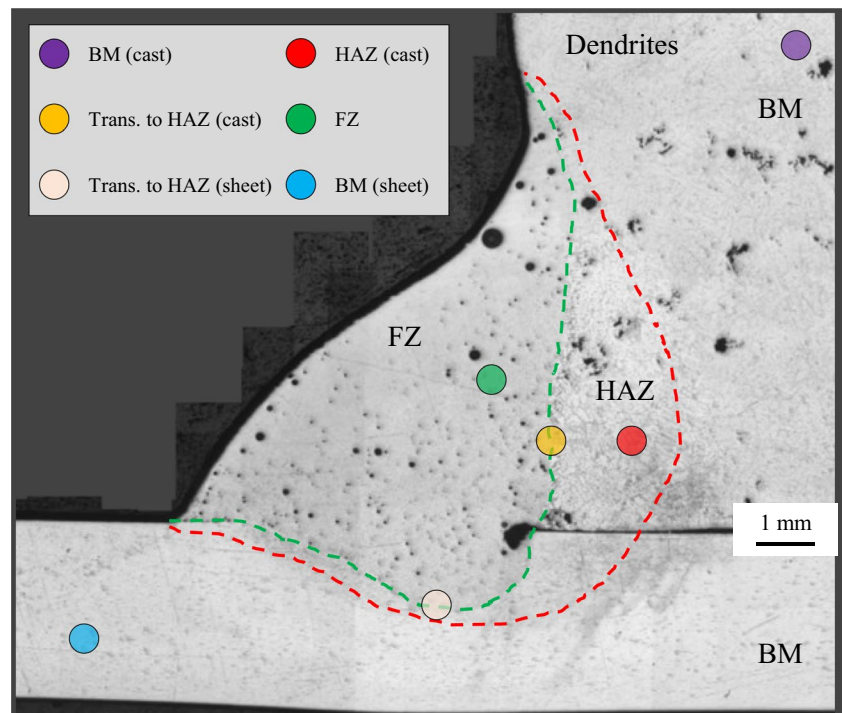

Fig. 6 Microstructures of a sheet/cast GMAW weld carried out with a travel speed of 12 mm/s: **a** BM (cast), **b** HAZ (cast), **c** transition region to HAZ (cast), **d** FZ, **e** transition region to HAZ (sheet) and **f** BM (sheet)

rolling direction with an average length and thickness of 80 μm and 15 μm (Fig. 6f).

Figure 7 shows the Vickers microhardness map of a sheet/cast GMAW weld. The cast shows an inhomogeneous hardness through its cross-section because of the heterogeneous microstructures. The average hardness is 80 HV, although peaks up to 110 HV can be obtained locally due to the Al–Si eutectic phase. In other regions, porosities make the material softer to the indenter penetration, showing a low apparent hardness (50–60 HV). The same consideration can be made for the weld bead, even if a more frequent hardness peak can be observed. This trend agrees with Hwang et al. [11], which also measured an increase of the hardness level in the FZ comparing to the BM in A356 joints (from 60 to 100 HV)

due to the elimination of the dendritic microstructure. The sheet shows an average hardness of 100 HV and a reduction to 80 HV in the HAZ. This hardness reduction is consistent with the literature, as Ramaswamy et al. [35] reported a value of 115 HV for the BM, which reduced to about 80 HV for the HAZ in AA6061-T6 arc joints.

3.2 FSW joint

Figure 8 shows the cross-sections of a sheet/cast FSW joint with the BM, HAZ, thermo-mechanical affected zone (TMAZ) and SZ. The SZ characterizes almost the entire weld, whose size is consistent with the tool size and plunge depth. Due to the higher material flow in the advancing side

Fig. 7 Typical Vickers microhardness map of a sheet/cast GMAW weld (travel speed of 12 mm/s)
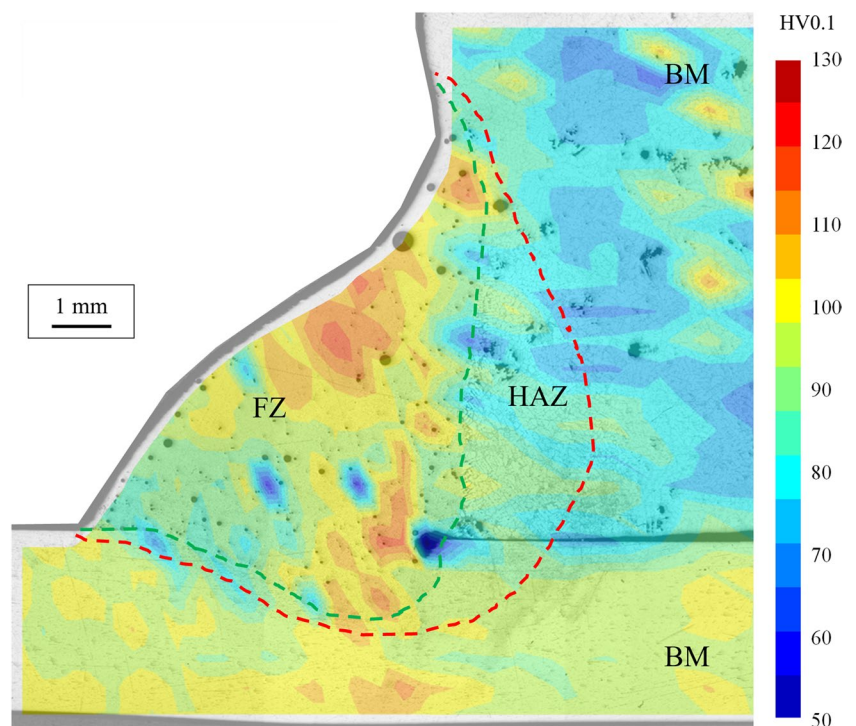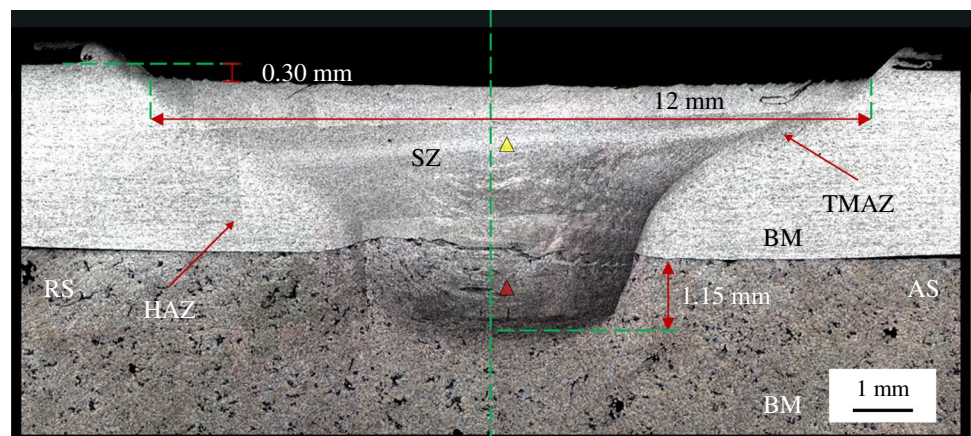

Fig. 8 Cross-section of a sheet/cast weld carried out via FSW. The coloured marks highlight the locations of the microstructures reported in Fig. 9

(AS), this area is characterized by stripes produced from the threaded pin profile. For the same reason, the SZ is not centred on the welding path, but it is shifted toward the AS. The extent of the TMAZ and HAZ is much more limited and slightly visible in the AS. On the other hand, they are not easily detected in the retracting side (RS) as the microstructure of the SZ continuously changes into the microstructure of the TMAZ for the same type of aluminium alloy [36]. Figure 8 does not show any weld defects in the joint cross-section. However, different defects can appear in a FSW joint as showed from Jayaraman et al. [37] for A356 (6 mm thick). For instance, the increase of the rotational speed up to 1400 rpm promoted the formation of a tunnel at the middle of the weld cross-section in the RS due to an abnormal stirring of the plasticized metal.

Figure 9 displays some characteristic areas of the FSW joint, as obtained from the locations highlighted by the coloured marks in Fig. 8. The SZ in the sheet side is characterized by an equiaxed grain structure with an average diameter of 5 μm, which rises to 10 μm in the cast part. The FSW process stirs and mixes the elongated grain structure visible in Fig. 6f for the sheet BM. Moreover, it eliminates the dendrites of the cast BM. According to Abbasi et al. [38], the grain size reduction occurring in the SZ is due to DRX during severe plastic deformation. The authors proposed a cellular automaton model which can analyze the dislocation accumulation map, nucleation and grain growth phase of DRX during the friction process. Eskandari et al. [39] found similar grain dimensions in their study for FSW between AA6061 and A390. Abbassi et al. [40] performed butt FSW on AA6xxx series alloys (3 mm thick) using different solid-state joining methods: conventional FSW, UWFSW and FSVW. SZ grain size decreases from about 57 μm for FSW to about 34 μm and about 23 μm respectively for FSVW and UWFSW.

Finally, the joint does not show noticeable pores in both the SZ of the sheet and cast parts because FSW drastically reduces its size thanks to its stirring and mixing action. This processing capability of FSW is particularly useful in materials which show an intrinsic porosity due to the peculiarities of their manufacturing process. For instance, Mahmoud et al. [41] realized A319 butt joints via FSW. The BM showed pores with a size between 100 and 1000 μm, while the joint cross-section did not show any evident porosity in the SZ. Similarly, Mirandola et al. [12] also confirmed this result for FSW joints of additively manufactured Scalamalloy®: pores derived from the additive process were noticed in the BM (size of 50–200 μm) but not in the SZ.

Figure 10 shows the Vickers microhardness map of a sheet/cast FSW weld. The cast shows a more homogeneous hardness moving towards the SZ with an average value of 100 HV. The recrystallization action imposed from the friction tool is more evident for the sheet part reaching a peak value of 130 HV close to the shoulder-affected zone. Finally, a drop in the hardness can be observed for the HAZ reaching 80 HV. However, excessive heat input can also be given

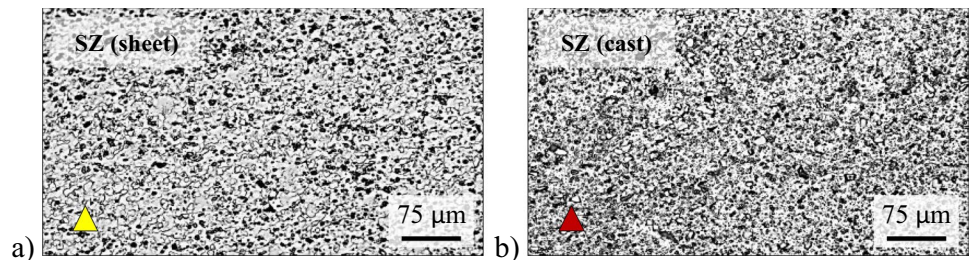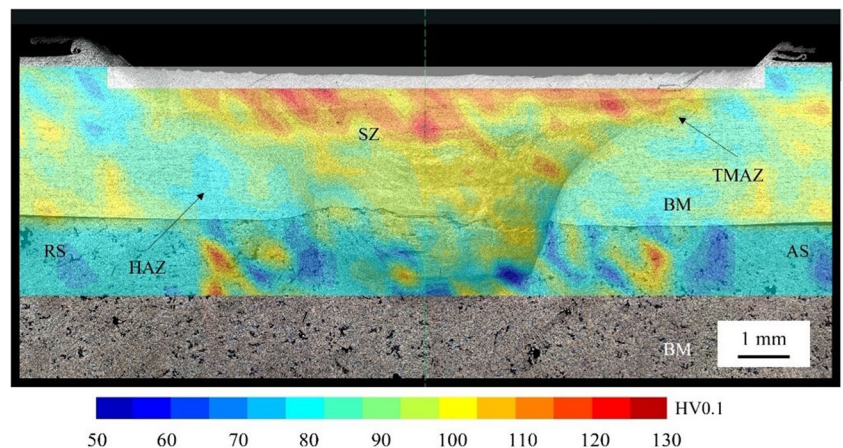**Fig. 9** Microstructures of a sheet/cast weld carried out via FSW: **a** SZ (sheet) and **b** SZ (cast)

Fig. 10 Typical Vickers microhardness map of a sheet/cast FSW weld

in FSW. For instance, Scialpi et al. [42] focused on butt AA6082-T6 welds. The authors measured a hardness of 100 HV for the BM and a drop to 70–80 HV for the entire weld area. In this study, conventional FSW was conducted at room temperature. However, Abdollahzadeh et al. [16] proved that heat plays an important role on the microstructure evolution and mechanical properties of FSW aluminium joints. For instance, the authors obtained a variation on the hardness level from 30 to 45 HV in the HAZ and from 50 to 85 HV in the SZ when changing the boundary condition (i.e. air, water or oil cooling) or variation in the FSW process (i.e. conventional or FSVW).

3.3 Porosity evaluation through 3D X-ray computed tomography

CT has been used to evaluate the porosity of the cast and the GMAW and FSW welded joints. The porosity of the cast has been measured by examining a reference parallelepiped having a size of about 20.6 mm $\times$ 25.3 mm $\times$ 10.5 mm (volume of 5472.38 mm^3). Figure 11 shows the distribution and volume of porosity. The CT revealed material and a porosity volume of 5393.19 mm^3 and 79.19 mm^3, respectively. Therefore, a porosity of 1.45% can be computed. A high number of pores equal to about 5900 can be noticed, with a single pore volume mainly belonging to the 0.001–0.065 mm^3 range.

A parallelepiped region of interest (ROI) throughout the cross-section of the GMAW beads has been subjected to CT (Fig. 12). The ROI has a cross-section of 12 mm $\times$ 11 mm (blue perimeter in Fig. 12) and a length of 50 mm along the
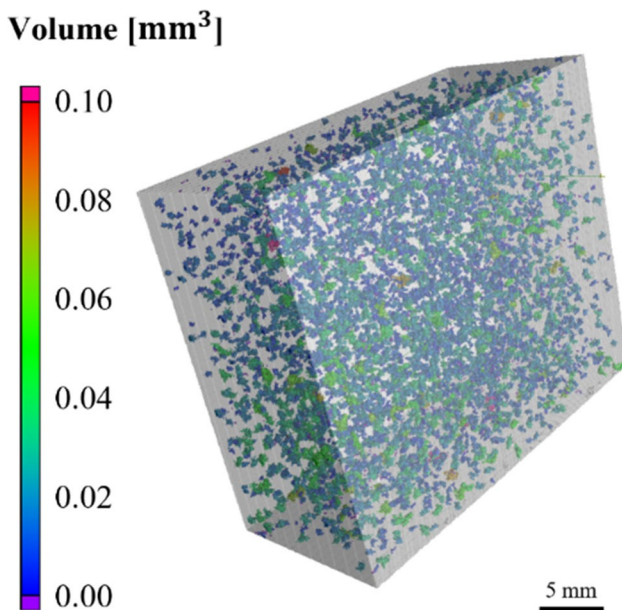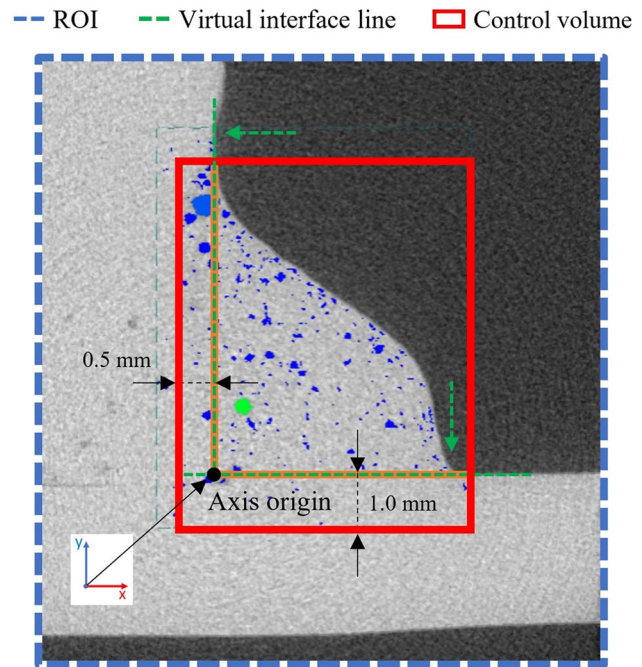

Fig. 12 Definition of the areas of interest for the 3D X-ray computed tomography analysis on the GMAW beads

weld bead. A control volume (red perimeter in Fig. 12) has been defined inside the ROI to measure the porosity within the weld bead. This region has been defined with an offset of 0.5 mm from the interface that divides (i) the weld bead and the cast part and with an offset of 1.0 mm from the interface that divides (ii) the weld bead and the sheet part. These two offsets have been defined to include the FZ inside the control volume.

Table 4 reports the porosity volume and number measured in the cast BM and the control volume defined in Fig. 12 for the GMAW beads. The amount of porosity is larger in the welded joints than in the cast BM. The rise of the travel speed plays a key role in increasing the porosity percentage, which goes from 1.80 to 5.12%. The number of pores also rises from about 10,000 at 12 mm/s to 20,000 at 14 mm/s. Moreover, the travel speed affects the number of pores with a volume higher than 0.10 mm^3, representing the 9.75% at 12 mm/s and the 32.98% at 14 mm/s of the total porosity. For sake of clarity, Fig. 13 shows the distribution and size of the pores inside the control volume of the GMAW beads at varying travel speeds.

Hooijmans and Den Ouden [43] provided a model to evaluate hydrogen absorption in the liquid metal during the GMAW of aluminium alloys. According to the authors, the hydrogen concentration in the melt-pool results from the dynamic balance between the inflow and the outflow of hydrogen. The inflow occurs through the interface between the arc and the melt-pool and between the melt-pool and the

Fig. 11 Distribution and volume of the pores inside the cast BM

Table 4 Porosity volume and number in the cast BM and GMAW beads defined from the control volume

Analysed part	Cast BM		AW—12 mm/s		AW—13 mm/s		AW—14 mm/s	
Pores (totality)	79.19 mm^3	1.45%	33.63 mm^3	1.80%	45.71 mm^3	2.68%	96.80 mm^3	5.12%
Control volume	5472.38 mm^3	-	1868.36 mm^3	-	1705.61 mm^3	-	1889.10 mm^3	-
Pore number	5908	-	10,315	-	9710	-	20,232	-
Pores: (> 0.1 mm^3)	0.47 mm^3	0.59%*	3.28 mm^3	9.75%*	7.73 mm^3	16.91%*	31.93 mm^3	32.98%*

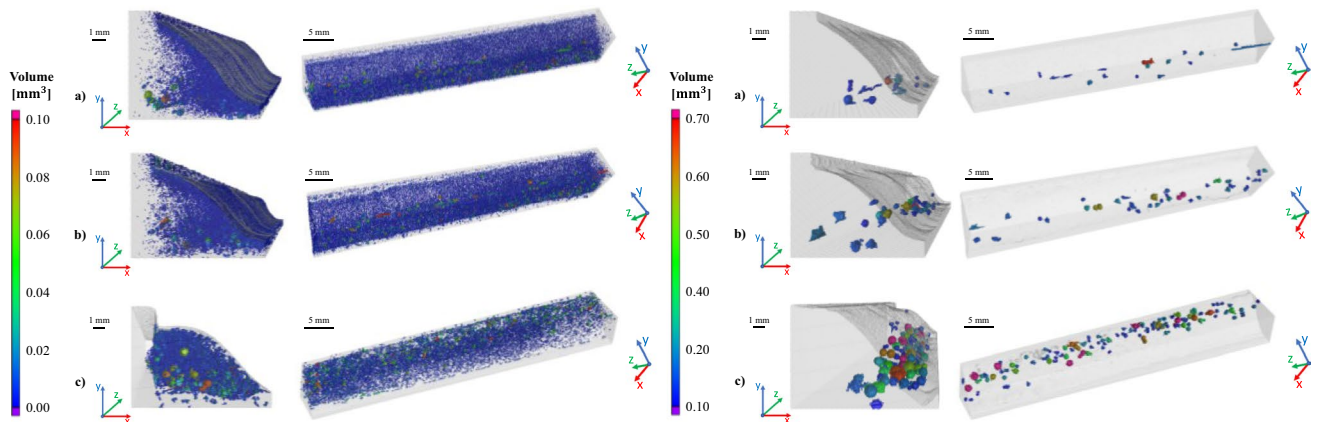*Percentage value computed respect to the total porosity

Fig. 13 Distribution and volume of the pores in the control volume of the GMAW welds obtained with a travel speed of **a** 12 mm/s, **b** 13 mm/s and **c** 14 mm/s

BM. Instead, the outflow occurs through the entire surface of the melt-pool. Moreover, the inflow dramatically increases with the amount of oxides on the metal and filler surfaces because aluminium oxide chemically reacts with water at high temperatures and produces hydrogen [19]. In this study, cleaning operations of samples were conducted in the same way. Therefore, the porosity generated from the reaction with the aluminium oxide is the same in all cases. The amount of pores coming from the cast BM is also similar in all cases because the same control volume was selected during 3D X-ray computed tomography (Fig. 12). It can be concluded that the faster cooling rate at the superior travel speed reduced the opening window in which pores could escape from it and raised the porosity of the joint. This phenomenon also promoted the growth of larger pores (i.e. volume > 0.10 mm^3) inside the weld. Moreover, according to the start-of-the-art literature, pores have a superior difficulty to escape from joints with a pronounced bead convexity [44]. Figure 4 shows that all welds show a convex shape close to the sheet BM and a concave shape close to the cast BM. The rise of the travel speed provocates a reduction in the concave region close to the BM hosting most of porosity.

Figure 13 also shows that most porosities with a volume below 0.05 mm^3 are located toward the external surface of the GMAW beads. On the other hand, pores with a volume higher than 0.3 mm^3 are mainly placed in the inner part

of the GMAW beads and towards the cast BM. Figure 14 focuses on the position of pores with respect to the x- and y-axis (see Fig. 12) and highlights an orange region evaluated inside the control volume of the GMAW beads. It contains at least 42% (with a maximum of 47%) of the pores revealed from the CT. The number of pores in the x-axis range [$- 0.5$; 0.0] ranges from 14 to 20%. This result suggests that the cast BM plays a key-role in forming porosity in the GMAW beads. These results agree with those from Liu et al. [25] for GMAW of A356 and AA7003. According to the authors, the pores in the cast became bubbles in melt-pool when this BM was heated during welding. With the fluctuation of the molten pool during the welding process, the smaller pores initially segregated and, subsequently, formed larger porosity.

Figure 15 shows the results of the CT analysis performed on the FSW joint. As expected, the FSW joint does not show porosity on the sheet side. However, a limited number of pores are visible in the SZ belonging to the previous cast BM, and they have a volume lower than 0.001 mm^3. Moreover, Fig. 15 highlights the footprint left by the friction tool in the cast BM. This result is due to the stirring and mixing action of the FSW tool against the previous porosity, as discussed for Fig. 8.

The data on porosity visible in Fig. 11 for the cast BM and in Fig. 13 for the GMAW beads were processed, and
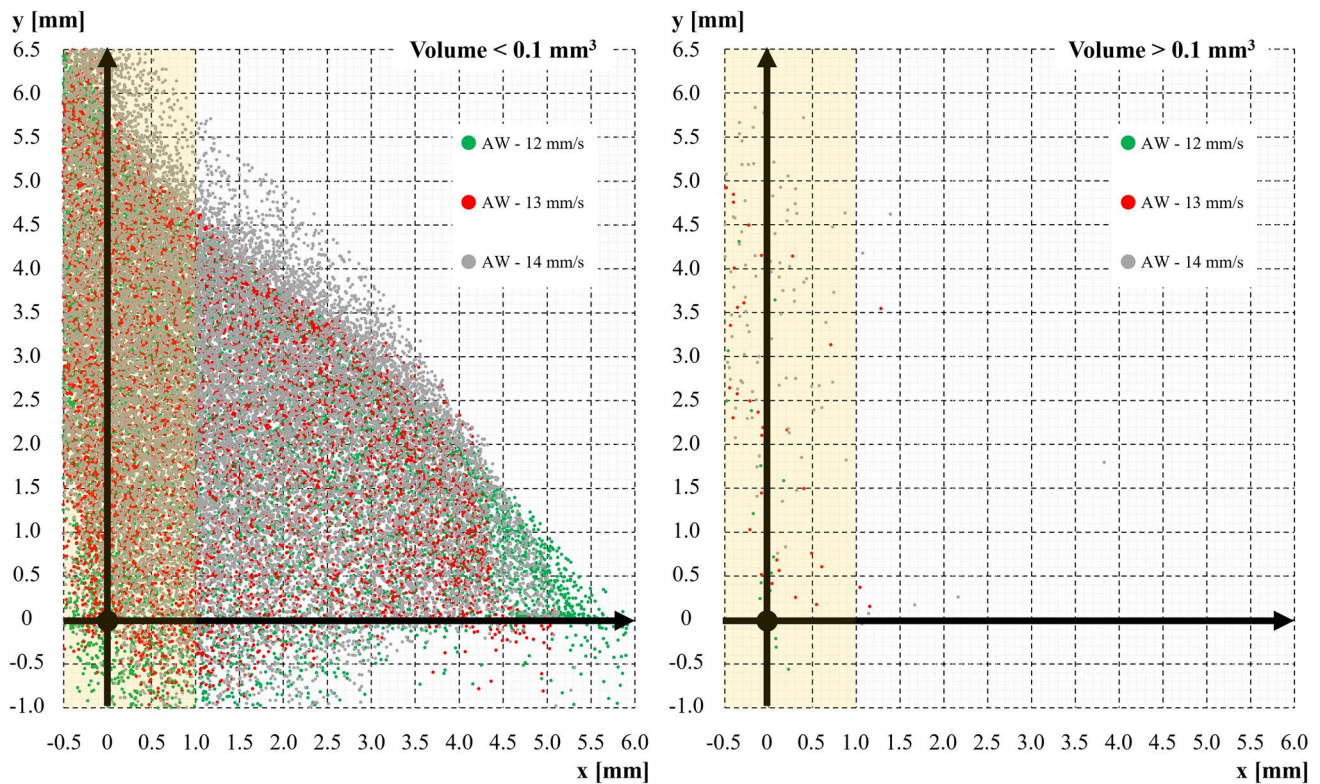
Fig. 14 Position of the pores with respect to the *x*- and *y*-axis in the control volume of the GMAW welds obtained with a travel speed of **a** 12 mm/s, **b** 13 mm/s and **c** 14 mm/s
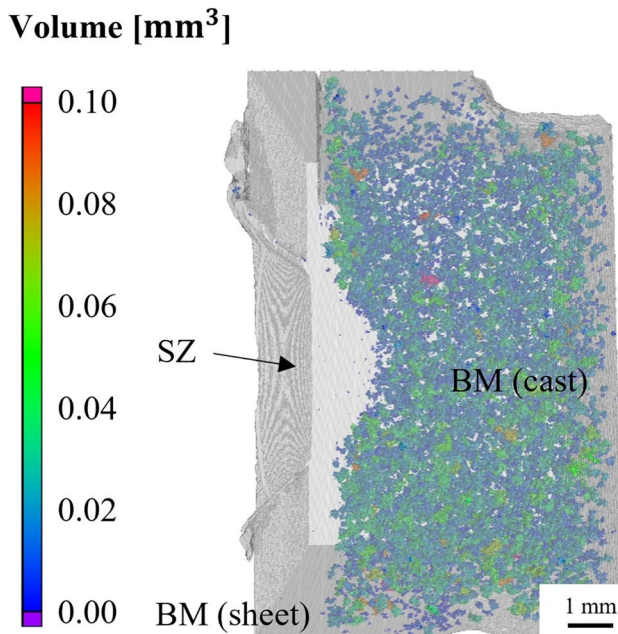

Fig. 15 Distribution and volume of the pores inside the FSW joint

the sphericity parameter and the equivalent diameter were computed using Eq. (1) and Eq. (2) from the VGDefX algorithm. Moreover, the algorithm also computed the maximum diameter, i.e. the maximum distance between two points on the surface of each pore. In Fig. 16, a strong hyperbolic connection can be noticed between the equivalent diameter and sphericity for the cast BM. The equivalent diameter of the pores goes from about 0.1 to 0.5 mm and a sphericity parameter remains in the 0.2–0.7 range.

On the other hand, the GMAW beads show pores with a higher equivalent diameter (up to 1.4 mm). Pore equivalent diameter and sphericity do not show a clear connection for the GMAW beads, especially for high pore diameters, even if a monotonically decreasing trend can be observed. For instance, Fig. 16 shows two pores for the GMAW bead obtained with a travel speed of 14 mm/s: a sphericity of about 0.75 is associated with a maximum diameter of 0.1 mm, while a sphericity of about 0.40 is associated with a maximum diameter of 2.1 mm. This decreasing trend agrees with different Ref.s found in the literature [45–47] for various thermal welded joints.
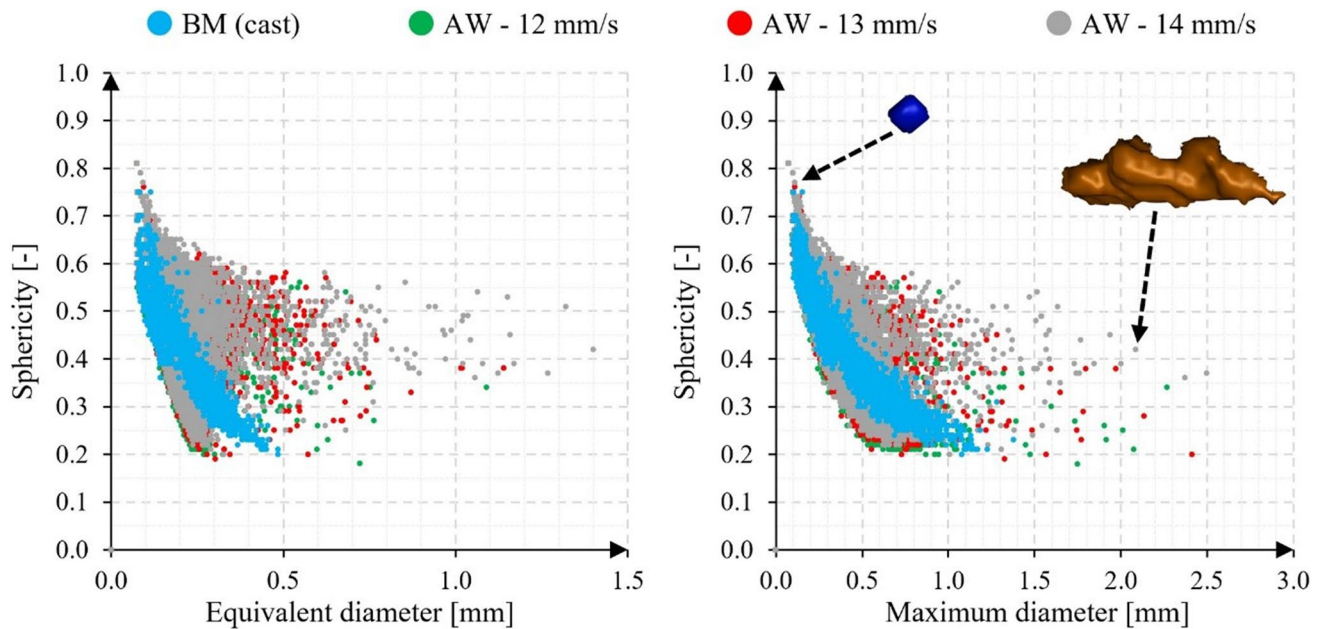
Fig. 16 Sphericity vs. equivalent diameter and maximum diameter

4 Conclusions

The main findings of this work can be summarized as follows:

- The CT investigation revealed that a porosity percentage of 1.45% characterizes the cast BM and that a strong hyperbolic relationship between pore equivalent diameters and sphericity is present for such pores.
- The CT investigation highlighted that the rise of travel speed in GMAW joints strongly increases the porosity level from 1.80% (at 12 mm/s) to 5.12% (at 14 mm/s). This phenomenon is due to the reduction of the opening window in which pores can escape. The increase of the travel speed also raises the percentage share of pores with volume higher than 0.10 mm^3, moving from 9.75 to 32.98% (computed referring to the total porosity).
- The region close to the cast BM contains at least 42% of the pores found in the investigated control volume, proving the contribution that the cast BM gives in the total joint porosity.
- In all cases, sphericity maintains a decreasing trend with the rise of the equivalent diameter, even if a weaker hyperbolic relationship is highlighted for GMAW joints, especially for high pore diameters.
- The joint cross-sections revealed the capability of FSW to eliminate the cast BM dendrites and to achieve a substantial reduction in the average grain size (from 30–100 to 5–10 μm). Moreover, no pores were noticed in macrographs of the FSW joint, which drastically reduces their size due to its stirring and mixing action.

This work demonstrates the strong potential of FSW for reducing weld porosity proving the necessity for a redesign of the battery-pack enclosures.

Data availability All data generated or analysed during this study are included within the article.

Code availability Not applicable.

Declarations

Consent to participate All authors agreed with the consent to participate.

Consent for publication All authors have read and agreed to the publication of the paper.

Competing interests The authors declare no competing interests.

References

1. EV-volumes. https://www.iea.org/reports/global-ev-outlook-2023/prospects-for-electric-vehicle-deployment. Accessed 14 Mar 2024

2. Cusenza MA, Bobba S, Ardente F et al (2019) Energy and environmental assessment of a traction lithium-ion battery pack for plug-in hybrid electric vehicles. J Clean Prod 215:634–649. https://doi.org/10.1016/j.jclepro.2019.01.056

3. Lander L, Tagnon C, Nguyen-Tien V et al (2023) Breaking it down: a techno-economic assessment of the impact of battery pack design on disassembly costs. Appl Energy 331:120437. https://doi.org/10.1016/j.apenergy.2022.120437

4. Lu L, Han X, Li J et al (2013) A review on the key issues for lithium-ion battery management in electric vehicles. J Power Sources 226:272–288. https://doi.org/10.1016/j.jpowsour.2012.10.060

5. Krüger C, Spohr S, Merdivan D, Urban P (2022) Avoiding structural redundancies between the vehicle body and the battery housing based on a functional integration approach. Automot Engine Technol 7:197–208. https://doi.org/10.1007/s41104-022-00106-8

6. Shui L, Chen F, Garg A et al (2018) Design optimization of battery pack enclosure for electric vehicle. Struct Multidiscip Optim 58:331–347. https://doi.org/10.1007/s00158-018-1901-y

7. Czerwinski F (2021) Current trends in automotive lightweighting strategies and materials. Materials (Basel) 14:6631. https://doi.org/10.3390/ma14216631

8. DuckerFrontier. https://www.duckercarlisle.com/. Accessed 4 Jan 2022

9. Novelis 6HS s650 datasheet. https://www.novelis.com/. Accessed 24 Jan 2023

10. Das A, Li D, Williams D, Greenwood D (2018) Joining technologies for automotive battery systems manufacturing. World Electr Veh J 9:22. https://doi.org/10.3390/wevj9020022

11. Hwang L, Gung C, Shih T (2001) A study on the qualities of GTA-welded squeeze-cast A356 alloy. J Mater Process Technol 116:101–113. https://doi.org/10.1016/S0924-0136(01)00829-9

12. Mirandola P, Lunetto V, Novel D et al (2023) Strength and microstructure of friction stir welded additively manufactured Scalmalloy® in as-welded and heat-treated conditions. J Manuf Process 97:1–11. https://doi.org/10.1016/j.jmapro.2023.04.051

13. Lunetto V, De Maddis M, Russo Spena P (2023) Pre-hole friction stir spot welding of dual-phase steels and comparison with resistance spot welding, conventional and pinless friction stir spot welding. Int J Adv Manuf Technol. https://doi.org/10.1007/s00170-023-12400-2

14. Tagawa T, Tahara K, Abe E et al (2014) Fatigue properties of cast aluminium joints by FSW and MIG welding. Weld Int 28:21–29. https://doi.org/10.1080/09507116.2012.715881

15. Abdollahzadeh A, Bagheri B, Abassi M et al (2021) Comparison of the weldability of AA6061-T6 joint under different friction stir welding conditions. J Mater Eng Perform 30:1110–1127. https://doi.org/10.1007/s11665-020-05379-4

16. Abdollahzadeh A, Bagheri B, Abbasi M et al (2021) A modified version of friction stir welding process of aluminum alloys: analyzing the thermal treatment and wear behavior. Proc Inst Mech Eng Part L J Mater Des Appl 235:2291–2309. https://doi.org/10.1177/14644207211023987

17. Bagheri B, Abbasi M, Hamzeloo R (2021) Comparison of different welding methods on mechanical properties and formability behaviors of tailor welded blanks (TWB) made from AA6061 alloys. Proc Inst Mech Eng Part C J Mech Eng Sci 235:2225–2237. https://doi.org/10.1177/0954406220952504

18. Abbasi M, Bagheri B, Abdollahzadeh A, Moghaddam AO (2021) A different attempt to improve the formability of aluminum tailor welded blanks (TWB) produced by the FSW. Int J Mater Form 14:1189–1208. https://doi.org/10.1007/s12289-021-01632-w

19. Vyskoč M, Sahul M, Sahul M (2018) Effect of shielding gas on the properties of AW 5083 aluminum alloy laser weld joints. J Mater Eng Perform 27:2993–3006. https://doi.org/10.1007/s11665-018-3383-x

20. Ardika RD, Triyono T, Muhayat N (2021) A review porosity in aluminum welding. Procedia Struct Integr 33:171–180. https://doi.org/10.1016/j.prostr.2021.10.021

21. Anyalebechi PN (2022) Hydrogen solubility in liquid and solid pure aluminum—critical review of measurement methodologies and reported values. Mater Sci Appl 13:158–212. https://doi.org/10.4236/msa.2022.134011

22. Zhang C, Bao Y, Zhu H et al (2019) A comparison between laser and TIG welding of selective laser melted AlSi10Mg. Opt Laser Technol 120:105696. https://doi.org/10.1016/j.optlastec.2019.105696

23. Chen S, Chi Y, Zhang P, Shi Y (2020) Mechanism to reduce the porosity during argon arc welding of aluminum alloys by changing the arc angle. Metals (Basel) 10:1121. https://doi.org/10.3390/met10091121

24. Kutsuna M, Yan Q (1999) Study on porosity formation in laser welds of aluminium alloys (Report 2). Mechanism of porosity formation by hydrogen and magnetism. Weld Int 13:597–611. https://doi.org/10.1080/09507119909447420

25. Liu W, Wang H, Lu F et al (2015) Investigation on effects of process parameters on porosity in dissimilar Al alloy lap fillet welds. Int J Adv Manuf Technol 81:843–849. https://doi.org/10.1007/s00170-015-7276-y

26. Brodarac Z, Stanic D (2014) Effect of the cooling rate on distribution of transition elements in the intermetallic Al-Mn-Fe-Si phase in AlSi9MgMn alloy. In: 71st world foundry congress: advanced sustainable foundry, WFC 2014. Bilbao, p 110056

27. Zovi A, Casarotto F (2007) Silafont-36, the low iron ductile die casting alloy development and applications. Metall Ital 99:33–38

28. ISO (2015) 18273:2015. Welding consumables - wire electrodes, wires and rods for welding of aluminium and aluminium alloys - Classification. https://www.iso.org/standard/64572.html

29. ISO 18273:2015. Welding consumables, Wire electrodes, wires and rods for welding of aluminium and aluminium alloys, Classification. https://www.iso.org/standard/64572.html

30. Li P, Nie F, Dong H et al (2018) Pulse MIG welding of 6061–T6/A356-T6 aluminum alloy dissimilar T-joint. J Mater Eng Perform 27:4760–4769. https://doi.org/10.1007/s11665-018-3528-y

31. Nie F, Dong H, Chen S et al (2018) Microstructure and mechanical properties of pulse MIG Welded 6061/A356 aluminum alloy dissimilar butt joints. J Mater Sci Technol 34:551–560. https://doi.org/10.1016/j.jmst.2016.11.004

32. Wang M, Da ZY, Hu H et al (2014) Tensile properties and microstructure of joined vacuum die cast aluminum alloy A356 (T6) and wrought alloy 6061. Adv Mater Res 939:90–97. https://doi.org/10.4028/www.scientific.net/AMR.939.90

33. ASTM International (2017) Standard test methods for Vickers hardness and Knoop hardness of metallic materials ASTM E92. https://www.astm.org/e0092-17.html

34. Wadell H (1935) Volume, shape, and roundness of quartz particles. J Geol 43:250–280. https://doi.org/10.1086/624298

35. Ramaswamy A, Malarvizhi S, Balasubramanian V (2019) Influence of post weld heat treatment on tensile properties of cold metal transfer (CMT) arc welded AA6061-T6 aluminium alloy

joints. J Mech Behav Mater 28:135–145. https://doi.org/10.1515/jmbm-2019-0015

36. Kopyściański M, Dymek S, Hamilton C et al (2017) Microstructure of friction stir welded dissimilar wrought 2017A and cast AlSi9Mg aluminum alloys. Acta Phys Pol A 131:1390–1394. https://doi.org/10.12693/APhysPolA.131.1390

37. Jayaraman M, Balasubramanian V (2013) Effect of process parameters on tensile strength of friction stir welded cast A356 aluminium alloy joints. Trans Nonferrous Met Soc China 23:605–615. https://doi.org/10.1016/S1003-6326(13)62506-6

38. Abbasi M, Bagheri B, Sharifi F (2021) Simulation and experimental study of dynamic recrystallization process during friction stir vibration welding of magnesium alloys. Trans Nonferrous Met Soc China 31:2626–2650. https://doi.org/10.1016/S1003-6326(21)65681-9

39. Eskandari M, Jamshidi Aval H, Jamaati R (2019) The study of thermomechanical and microstructural issues in dissimilar FSW of AA6061 wrought and A390 cast alloys. J Manuf Process 41:168–176. https://doi.org/10.1016/j.jmapro.2019.03.040

40. Abbasi M, Abdollahzadeh A, Bagheri B et al (2021) Study on the effect of the welding environment on the dynamic recrystallization phenomenon and residual stresses during the friction stir welding process of aluminum alloy. Proc Inst Mech Eng Part L J Mater Des Appl 235:1809–1826. https://doi.org/10.1177/14644207211025113

41. Mahmoud TS, Gaafer AM, Khalifa TA (2008) Effect of tool rotational and welding speeds on microstructural and mechanical characteristics of friction stir welded A319 cast Al alloy. Mater Sci Technol 24:553–559. https://doi.org/10.1179/174328408X294116

42. Scialpi A, De Filippis LAC, Cavaliere P (2007) Influence of shoulder geometry on microstructure and mechanical properties of friction stir welded 6082 aluminium alloy. Mater Des 28:1124–1129. https://doi.org/10.1016/j.matdes.2006.01.031

43. Hooijmans JW, Den Ouden G (1997) A model of hydrogen absorption during GTA welding. Weld J 76:264–268

44. Da Silva CLM, Scotti A (2006) The influence of double pulse on porosity formation in aluminum GMAW. J Mater Process Technol 171:366–372. https://doi.org/10.1016/j.jmatprotec.2005.07.008

45. Bandi B, Dinda SK, Kar J et al (2018) Effect of weld parameters on porosity formation in electron beam welded Zircaloy-4 joints: X-ray tomography study. Vacuum 158:172–179. https://doi.org/10.1016/j.vacuum.2018.09.060

46. Dinda SK, Warnett JM, Williams MA et al (2016) 3D imaging and quantification of porosity in electron beam welded dissimilar steel to Fe-Al alloy joints by X-ray tomography. Mater Des 96:224–231. https://doi.org/10.1016/j.matdes.2016.02.010

47. Das D, Dinda SK, Das AK et al (2022) Study of micro-porosity in electron beam butt welding. Int J Adv Manuf Technol 121:4583–4600. https://doi.org/10.1007/s00170-022-09359-x